# Electrospun Ternary Composite Metal Oxide Fibers as an Anode for Lithium-Ion Batteries

*JinKiong Ling[1,2], Chelladurai Karuppiah[3], Santanu Das[4], Izan Izwan Misnon[1,2], Mohd Hasbi Ab. Rahim[1,2], Chun-Chen Yang[3,5,6]\* and Rajan Jose[1,2]\**

[1]Center of Advanced Intelligent Materials, Universiti Malaysia Pahang, Kuantan, Malaysia, [2]Faculty of Industrial Sciences and Technology, Universiti Malaysia Pahang, Kuantan, Malaysia, [3]Battery Research Centre for Green Energy (BRCGE), Ming Chi University of Technology, New Taipei City, Taiwan, [4]Department of Ceramic Engineering, Indian Institute of Technology (Banaras Hindu University), Varanasi, India, [5]Department of Chemical Engineering, Ming Chi University of Technology, New Taipei City, Taiwan, [6]Department of Chemical and Materials Engineering, Chang Gung University, Taoyuan, Taiwan

Nickel–cobalt–manganese oxides (NCMs) are widely investigated as cathode materials for lithium-ion batteries (LIBs) given their beneficial synergistic effects of high storability, electrical conductivity, and stability. However, their use as an anode for LIBs has not been adequately addressed. NCM nanofibers prepared using the multi-needle electrospinning technique are examined as the anode in LIBs. The NCM nanofibers demonstrated an initial discharge capacity of ~1,075 mAh g$^{-1}$ with an initial capacity loss of ~42%. Through controlling the conductive additive content, the initial discharge capacity can be further improved to ~1810 mAh g$^{-1}$, mostly attributing to the improved interfiber connectivity supported by the significant lowering of impedance when the amount of conductive additive is increased. This study also reveals that the conventional ratio of 80:10:10 wt% (active materials:additives:binder) is not optimal for all samples, especially for the high active surface area electrospun nanofibers.

Keywords: secondary batteries, rechargeable, quaternary metal oxide, composite, vapor grown carbon fiber (VGCF), super P, conductive additives

## INTRODUCTION

Ever since its discovery in the beginning of 1980s, rechargeable lithium-ion battery (LIB) attracted tremendous attention as one of the crucial elements to the decarbonized energy sector for a sustainable society (Mizushima et al., 1980; Goodenough, 2018). Following its commercialization by Sony, efforts are mostly focused on developing cathode materials with improved electrochemical properties, such as nickel–lithium-rich nickel–cobalt–manganese oxide (NCM) and nickel–cobalt–aluminum oxide (NCA) (Song et al., 2020; Wang et al., 2020; Xu et al., 2020) (Tolouei et al., 2019; Zhang et al., 2019; Guanjie Li et al., 2020) as well as high potential spinel LiMn$_{1.5}$Mn$_{0.5}$O$_4$ and olivine LiMPO$_4$ (where M = Co, Ni, Mn) (Chemelewski et al., 2013; Liang et al., 2020; Ling et al., 2021a) materials. Recently, demand to deploy LIBs in long-mileage electric vehicles as well as smart energy grid applications urged the enhancement of their energy density. With development of cathode materials for the lithium-ion battery showing sign of saturation, especially nickel-rich layered materials, the next measure would be to develop the anode with improved electrochemical performance.

The past decade has witnessed significant amount of work in developing conversion- and alloying-type anodes, with the latter capable of delivering 2,500–3000 mAh g$^{-1}$ compared to

300–350 mAh·g$^{-1}$ of the conventional graphite anode (Casimir et al.2016; Zhang et al.2020). However, alloying-type anodes suffered from extreme volume changes during lithiation/delithiation (300–400 vol.%), resulting in poor cycling stability (Zuo et al.2017; Yang et al.2020). Fortunately, improvement in cycling stability was demonstrated through compositing with graphite or rGO (Yim et al.2013; He et al.2021), with the carbonaceous materials buffering the volume expansion during lithiation and enhancing the mechanical integrity (Moon et al.2021). Similar techniques were also reported in numerous occasions, demonstrating improved electrochemical properties of wide variety of anode materials—hinting its crucial role in high energy density LIBs. We have previously reported synergistic behavior in the $SnO_2$–$TiO_2$ composite nanofibers anode, demonstrating the benefits of adopting composite materials as well as the importance of tuning the chemical composition to draw maximum electrochemical performance from the composite material (Ling et al. 2021 Ling et al.2021b). Compositing $SnO_2$–CuO materials also demonstrated synergistic effect of improved electronic conductivity from $SnO_2$ as well as higher redox potential from CuO (JinKiong and Jose 2021). Similar observation can also be made on binary, ternary, or even quaternary composite metal oxides, which are thoroughly reviewed in previous publications (Cao et al.2017; Fang et al.2020). In fact, such synergistic behavior is widely adopted in the NCM cathode material also, with nickel and cobalt improving the capacity and electrical conductivity of the material, respectively, whereas manganese functions as the pillar to stabilize the crystal structure during the lithiation/delithiation process (Musuvadhi Babulal et al.2021; Seenivasan et al.2021; Wu et al.2021). Surprisingly, despite having attractive synergistic properties, NCM has not been extensively studied as the anode materials for LIBs. To the best of our knowledge, the usefulness of NCM as the anode of LIB is published only once by Solmaz et al., demonstrating a gravimetric discharge capacity of 968 mAh g$^{-1}$ at 100 mAh g$^{-1}$ (Solmaz et al.2020). However, Solmaz et al. focused on the effect of the hydrothermal parameter on the structural and electrochemical performance of the NCM anode, without further dwelling into correlating the structure properties of these materials with its electrochemical performance.

We synthesized nickel–manganese–cobalt oxide nanofibers (nfs-NCM) using the large-scale multi-needle electrospinning technique and studied its electrochemical performance as anodes for LIBs. Nanofiber morphology was chosen in this study, considering its anisotropic charge transport properties and higher surface area, which are the two crucial factors for achieving anode material with high specific capacity (Fan et al., 2017; Cong et al., 2021). The electrochemical properties of the nf-NCM were investigated through fabricating a CR2032 half-cell with lithium metal as the counter and reference electrode. Through comparing the cathodic and anodic peak with the crystal structure of the nf-NCM, the structural–electrochemical properties correlation could be achieved. The sample shows a typical conversion-type charge storage mechanism, considering the absence of the alloying process during (de)charging in both cyclic-voltammetry and galvanostatic charge–discharge profile.

The content of additive carbon was also varied, unveiling the relationship between the amount of additive carbon and the surface area of the nf-NCM. Our results demonstrate that the nf-NCM could serve as a promising anode material for lithium-ion batteries with further treatments to improve its cycling stability.

# EXPERIMENTAL SECTION

## Electrospinning of Nickel–Cobalt–Manganese Oxide Nanofibers

For the preparation of electrospinning polymeric solution, 15 wt% polyvinylpyrrolidone (5 g, Mw ~1,300,000 by LS, Sigma-Aldrich) was dissolved in N'N-dimethylformamide (32 ml, analytical grade, Emsure$^{®}$) through magnetic stirring for 2 h at room temperature and obtained a homogenous mixture. Then, 1 M metal precursors (consisting of 10 mmol nickel chloride, R&M Chemicals, 5 mmol cobalt chloride, R&M Chemicals, and 5 mmol manganese chloride, Bendosen) were subsequently dissolved in the polymeric mixture while stirring. The mixture was further stirred overnight at room temperature to obtain a homogenous blend. The blend was loaded into a 50-CC Terumo syringe, which was connected to a 20-needle (0.70 × 38 mm) injector for electrospinning. The electrospun nanofiber mat was collected on a grounded aluminum foil. The electrospinning process was carried out by applying a potential difference of 50 kV across the needles and the aluminum foil collector, with a solution feeding rate of 50 ml h$^{-1}$ (equivalent to 2.5 ml h$^{-1}$ per needle), under a strictly controlled chamber environment (~40% relative humidity and 30°C temperature). The electrospun mat collected on the aluminum foil was first calcined for 3 h at 600°C in air with a heating rate of 1°C min$^{-1}$. The obtained powder was then collected into an alumina crucible, followed by annealing for another 6 h at 850°C in air with a heating rate of 1°C min$^{-1}$. The final powder, denoted as nf-NCM, was used without further processing and purification.

## Device Fabrication

The prepared nf-NCM was used as the anode electrode, which was prepared through a simple slurry casting technique. The slurry was prepared by mixing the nf-NCM powder, conductive Super P additive, and poly(vinylidene fluoride) binder at a weight ratio of 80:10:10 wt%. All the solid powder was dissolved in 1-methyl-2-pyrrolidinone (NMP) at a weight ratio of 30:70% to achieve favorable consistency for casting. For the anode electrode with a higher ratio of conductive additive, the ratio of nf-NCM powder, conductive additives, and PVDF binder was manipulated to 70:20:10 wt%, denoted as nf-NCM(P20). Some amount of conductive carbon Super P was replaced by vapor-grown carbon fiber (VGCF), resulting in two more anodes with a weight ratio (nf-NCM:Super P:VCGF:PVDF) of 70:15:5:10 and 70:10:10:10, denoted as nf-NCM(v5) and nf-NCM(v10), respectively. The prepared slurry was casted on the copper foil

(which was etched with sulfuric acid to improve slurry adhesion) with a blade height of 200 μm with a coating speed of 2 mm s$^{-1}$. The electrode was dried at 80°C overnight, followed by 120°C for 1 h before punching into circular disc shape (13 mm in diameter) and roll-pressed to a density of 2 g cm$^{-3}$. All the prepared anodes have an active mass loading of ~1.5 mg. The CR2032 lithium-ion half-cell was fabricated in an argon-filled glove box, with the prepared electrode as the anode, lithium metal as both the counter and reference electrode, and Celgard 2,400 polypropylene film as the separator. LiPF$_4$ (1.0 M) in 1:1 (vol %) ethylene carbonate:diethyl carbonate was used as the electrolyte. Prior to electrochemical measurement, the cell was left to rest for 2 days to ensure complete wetting of the anode.
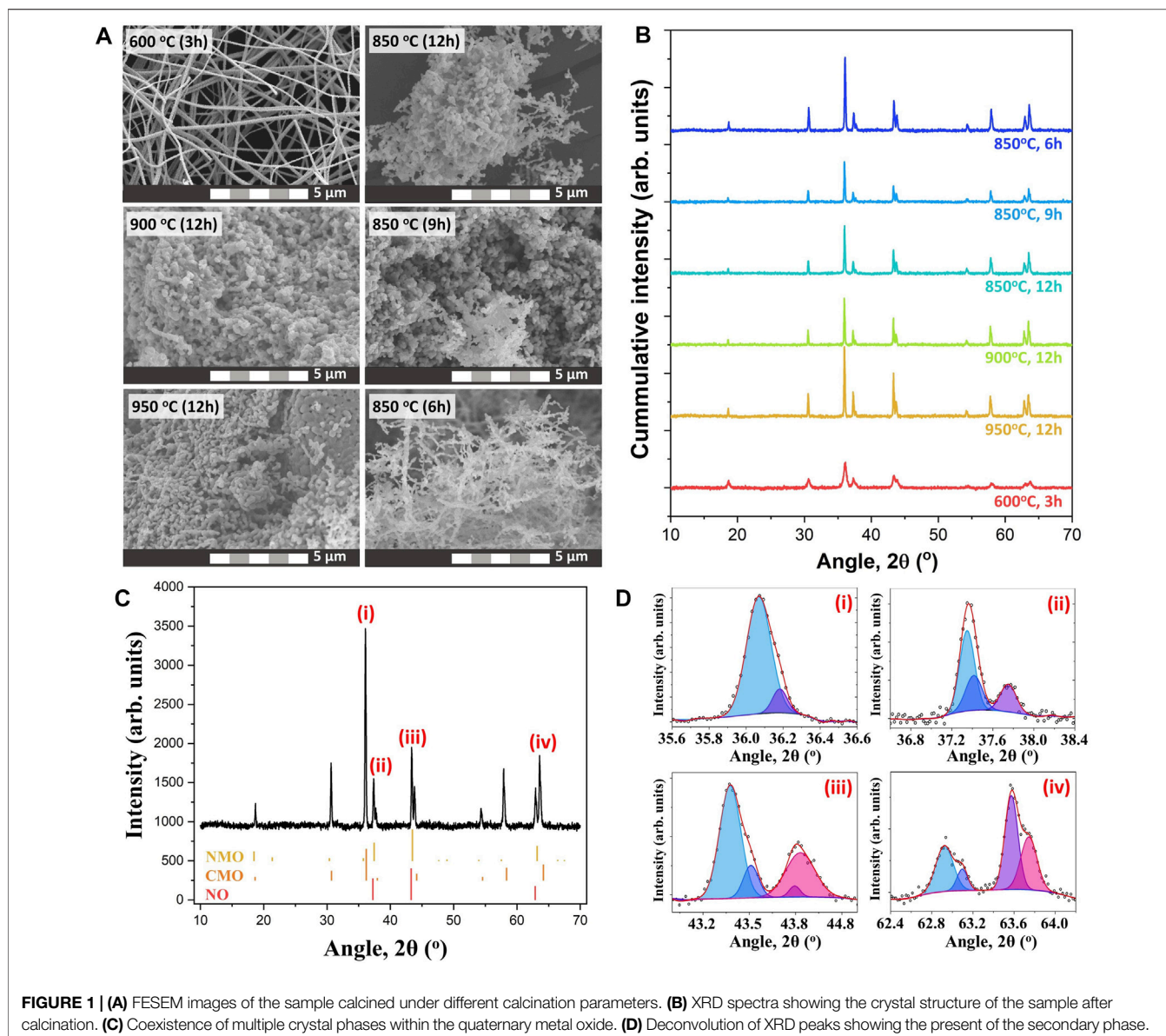
## Material Characterization

Field-emission scanning electron microscopy (FESEM, JOEL, JSM-7800F, United States, operating at 30 kV) was used to study the morphology of the nf-NCM with an emission source positioned 10 mm above the sample. A thin layer of platinum was coated on top of the sample to minimize distortion due to surface charge accumulation during FESEM observation. The elemental composition of all the samples was also studied using energy-dispersive X-ray spectroscopy (EDX) attached to the FESEM unit. X-ray diffraction spectroscopy (XRD, Brunker/D2 Phaser), with Cu Kα radiation (λ = 1.5406 Å) was employed to study the crystal structure of the nf-NCM. The XRD spectrum was recorded in the 10–70° range, with a step-size of ~0.02° and scanning speed of ~0.5° min$^{-1}$. X-ray photoelectron spectroscopy (XPS, PHI Quantera II, Physical Electronics) was used to analyze the surface chemistry of the sample. For XPS analysis, the nf-NCM paste was prepared by mixing with ethyl cellulose and α-terpineol at a weight ratio of 1:4.05:0.5 wt%, followed by doctor-blading on the bare microscopic glass and calcined at 500°C for 1 h. The spectra for the coated sample were recorded from 0-1,100 eV with Al (λ = 117.4 eV) as an emission source. The core level of each element was scanned at the binding energy range of 520–540, 630–660, 770–810, and 840–890 for O 1s, Mn 2p, Co 2p, and Ni 2p, respectively. The cyclic-voltammetry (CV) and electrochemical impedance spectroscopy (EIS) were obtained using a multichannel potentiostat/galvanostat (Autolab workstation with an M101 module FRA32M attachment, Metrohm). The CV of the samples was measured from 0–3 V at a scan rate of 0.1 mV s$^{-1}$, whereas the EIS spectra were obtained in the frequency range of 1–5 mHz; AC amplitude of ~10 mV at the open-circuit potential (OCP) of the cells was measured using the in-built OCP procedure of NOVA 1.10 software and fitted using Z-view software. The coin cells were subjected to five cycles of galvanostatic charged/discharged at 100 mA g$^{-1}$ as the formation cycle using the potentiostat–galvanostat.

## RESULTS AND DISCUSSION

The nf-NCM in this work was prepared via multi-needle electrospinning, followed by post-annealing for phase formation and to improve its crystallinity. Previous work has demonstrated that high temperature calcination (850–900°C) is required for maximum electrochemical performance for the lithium–nickel–cobalt–manganese oxide cathode (Kim 2012; Chen et al., 2021). However, the electrospun nanofiber mat can only be calcined to 600°C to prevent decomposition of the aluminum foil (collector), which would lead to contamination of the nf-NCM. Therefore, the nf-NCM was first calcined at 600°C for 3 h, with the powder collected into a crucible and subsequently calcined at higher temperature. The FESEM image (**Figure 1A**) confirmed the nanofiber morphology with a diameter of 312.9 ± 82.1 nm for samples calcined at 600°C for 3 h, although with poor crystallinity (**Figure 1B**). Further calcination is required to achieve highly crystalline electrodes with higher rate capability and longer stability (Yue et al., 2018). Two main criteria were considered while deciding the second calcination parameters: 1) the improvement in crystallinity of the sample and 2) the preservation of the morphology. The heating rate was kept constant at 1°C min$^{-1}$. The nf-NCM was first calcined at 850, 900, or 950°C for 12 h. The XRD spectra (**Figure 1B**) showed significant improvement in crystallinity, with the sample calcined at 950°C, showing the sharpest peak compared to 900 and 800°C samples. However, the fiber morphology was completely disintegrated when calcined at elevated temperature, most likely due to the Ostwald ripening effect that leads to fusion between adjacent fibers. Surprisingly, some fibers survived the Ostwald ripening process after being calcined at 850°C for 12 h. Therefore, 850°C was chosen to be the annealing temperature, where the calcination duration was reduced to minimize the Ostwald ripening leading to morphology disintegration. Among 12, 9, and 6 h, the latter showed the sharpest peak from the XRD spectra (**Figure 1B**), indicating the best crystallinity achieved among all the samples. The measurement parameters during XRD analysis were identical; therefore, increase in the peak intensity can be related to better crystallinity. To our surprise, most features of the fiber morphology were preserved after calcining at 850°C for 6 h (**Figure 1A**). Elemental analysis using EDS, as shown in **Figure 2A**, concluded the ratio between nickel, cobalt, and manganese to be 2:1:1, identical to the ratio designated during sample preparation. Elemental mapping further confirmed that all transition metals were homogeneously distributed throughout the nanofibers (**Figure 2B**).

Surprisingly, the XRD spectrum of nf-NCM does not correlate well with any single-material system, indicating the existence of multiple crystal phases within the quaternary metal oxide (**Figure 1C**). Fitting using DIFFRAC.SUITE software (Bruker) confirmed the existence of the crystal phase of Co$_2$MnO$_4$ and Ni$_6$MnO$_8$/NiO phases. The diffraction peaks positioned at 2θ ~18.9° (111), ~30.8° (220), ~36.2° (311), ~37.9° (222), ~44.0° (400), ~54.5° (422), ~58.1° (511), and ~63.8° (440) matched well with the Co$_2$MnO$_4$ phase (JCPDS no. 23–1,237; *fm-3m* cubic structure). However, the standard XRD spectrum of the Ni$_6$MnO$_8$ phase (JCPDS no. 42–479) overlays that of the NiO phase (JCPDS no. 47–1,049), posting difficulties in determining the presence of NiO phases. The area under the crystalline peaks can be used to compare and identify the fraction of each crystalline phase. To do so, we first assume that the peaks centered at 2θ ~37°, ~43°, and ~63° corresponded to the crystal planes (111), (200), and

**FIGURE 1 | (A)** FESEM images of the sample calcined under different calcination parameters. **(B)** XRD spectra showing the crystal structure of the sample after calcination. **(C)** Coexistence of multiple crystal phases within the quaternary metal oxide. **(D)** Deconvolution of XRD peaks showing the present of the secondary phase.

(220) of NiO (space group *fm-3m*), respectively. The ratio of Ni:Co: Mn was calculated to be 18.2:36.4:45.4, which is significantly different from the ratio obtained from EDS (**Figure 2A**). The difference in ratio can be attributed to the coexistence of both $Ni_6MnO_8$ and NiO phases within the samples, which is further confirmed through XPS analysis as detailed in the next paragraph. Surprisingly, a secondary peak can be deconvoluted at a higher angle after second calcination (**Figure 1D**), indicating the formation of secondary phases besides $Co_2MnO_4$, $Ni_6MnO_8$/NiO. Such secondary peak was attributed to the oxidation of $Ni^{2+}$ to $Ni^{3+}$ as well as $Co^{2+}$ to $Co^{3+}$ (Manthiram 2020), where the smaller ionic radii of $Ni^{3+}$ and $Co^{3+}$ shrank the lattice parameter and shifted their respective peaks to a higher angle. The existence of Co and Ni at +3 oxidation state can also be observed in XPS spectra (**Figure 2C**).

The XPS spectra were recorded using Al Kα radiation; the high-resolution XPS peaks were fitted to symmetric Gaussians

using Origin 8.0 software without any constraints on the center position, the FWMH, and the area of the peaks. The XPS background was defined using the Shirley–Vegh–Salvi–Castle (SVSC) approach (Herrera-Gomez et al., 2014). All the recorded XPS core level spectra were calibrated according to the peak center of C 1s (**Figure 2C**) to minimize shifting in binding energy due to space charge accumulation. Compared to 284.8 eV for C 1s (Li et al., 2019), the nf-NCM samples showed ~2.0 eV higher binding energy. The deconvoluted core level spectrum for each element is showed in **Figure 2D**. A 17.5 eV binding energy difference between peaks (i) and (iii) for Ni 2p corresponded to $Ni^{2+}$ oxidation states (Dubey et al., 2018). The 15.6 eV binding energy difference between peaks (v) and (vii) for Co 2p can be attributed to $Co^{2+}$ oxidation state. Given the fact that element with a higher oxidation state possessed higher binding energy, peaks for (i') and (iii') as well as (v') and (vii')
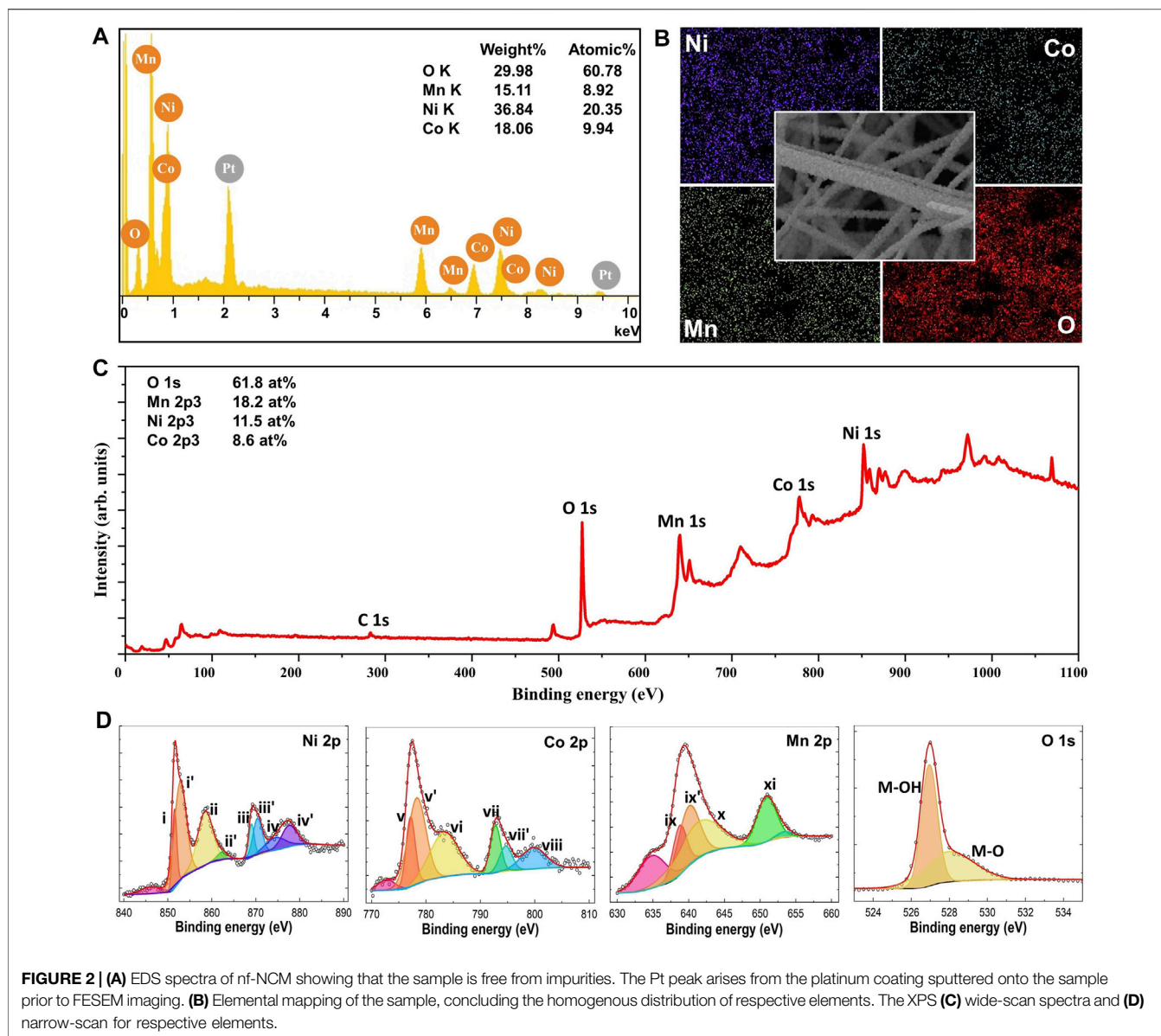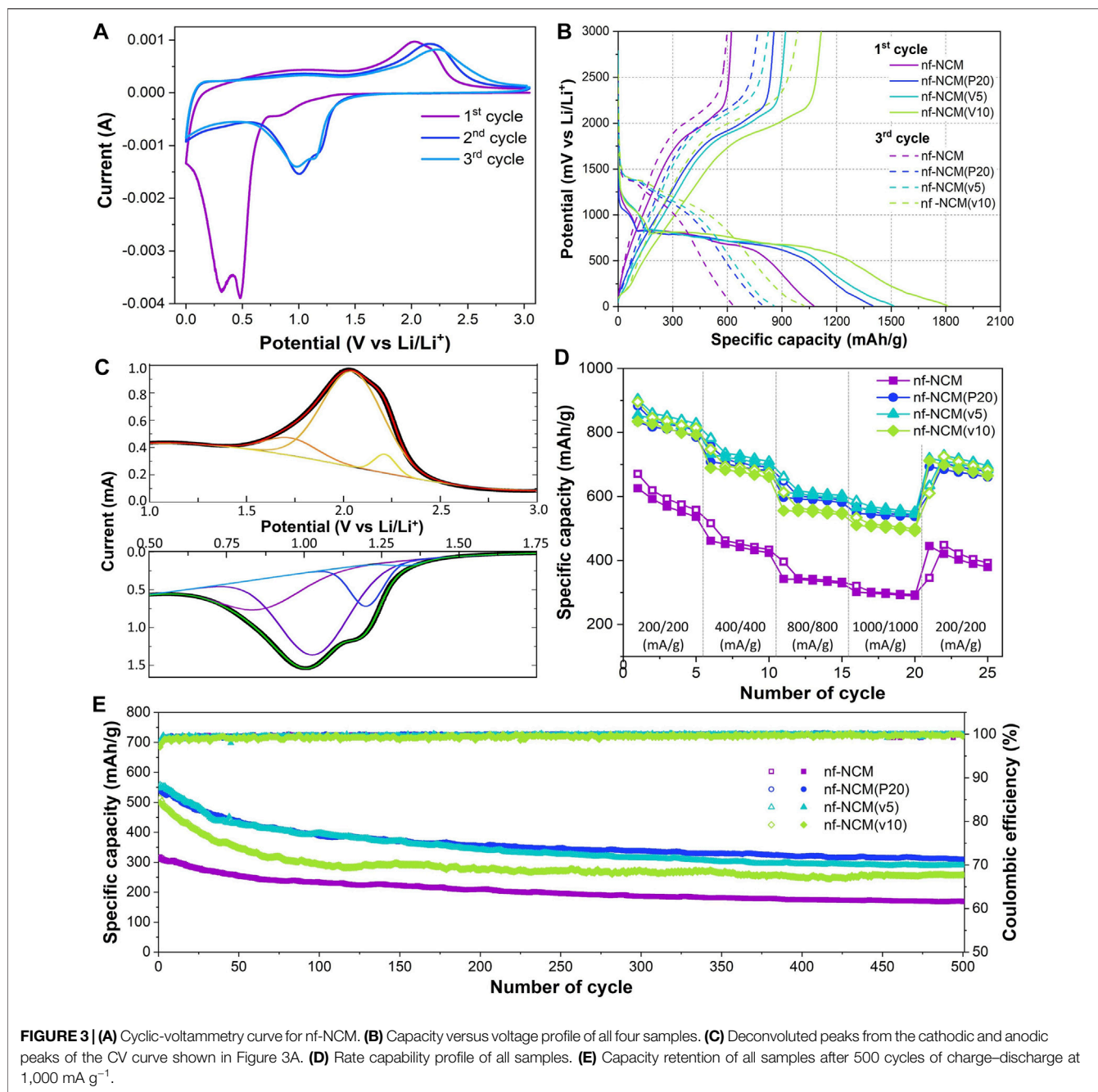
**FIGURE 2 | (A)** EDS spectra of nf-NCM showing that the sample is free from impurities. The Pt peak arises from the platinum coating sputtered onto the sample prior to FESEM imaging. **(B)** Elemental mapping of the sample, concluding the homogenous distribution of respective elements. The XPS **(C)** wide-scan spectra and **(D)** narrow-scan for respective elements.

can be attributed to $Ni^{3+}$ and $Co^{3+}$, respectively. The presence of $Ni^{3+}$ and $Co^{3+}$ matched well with the observation of secondary peak in the XRD spectra. We compared the fraction of $Ni^{2+}$, $Ni^{3+}$, $Co^{2+}$, and $Co^{3+}$ using the peak area, revealing high similarity between XRD (16.5:33.0:41.3:9.2%) and XPS (18.9:33.1:38.0: 10.0%) data. As for Mn 2p core level, the difference in binding energy between (ix–xi)/(ix'–xi) are 12.1/10.9 eV. Peaks (ix') and 11) can be assigned to $Mn^{4+}$ oxidation state, where the deconvoluted peak (ix) can be attributed to $Mn^{3+}$ oxidation state (Bulavchenko et al., 2018). The reduction of $Mn^{4+}$ to $Mn^{3+}$ could be the stabilizing act to neutralize charge changes when both $Ni^{2+}$ and $Co^{2+}$ were oxidized to $Ni^{3+}$ and $Co^{3+}$ (He et al., 2020; Wangda Li et al., 2020). The O 1s core level can be deconvoluted into two individual peaks, with peaks at 530.0 and 529.0 eV, corresponded to M–O–M and M–O–H bonding, respectively.

The cyclic voltammetric curves for nf-NCM at 0.1 mV s$^{-1}$ are shown in **Figure 3A**, and its first five galvanostatic charge–discharge cyclings at 100 mA h g$^{-1}$ are in **Figure 3B**. The nf-NCM recorded an initial discharge capacity of ~1,074.8 mA h g$^{-1}$, followed by ~623.0 mA h g$^{-1}$ charging capacity, showing an initial capacity loss of ~42%. The potential plateau from the charge–discharge curve is in line with the cyclic–voltammetric curve. The potential plateau at 0.8 V during the first discharging corresponded with the broad cathodic (reduction) peak at 0.85 V, which can be attributed to the solid–electrolyte interface (SEI) formation. The intense peak at <0.7 V can be attributed to the conversion of quaternary metal oxide to metal (reaction #1) as well as irreversible phase transition (reaction #2). This intense peak disappeared during the subsequent cycles, indicating that the irreversible phase transition could be one of the main contributors to the large
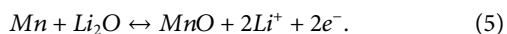
**FIGURE 3 | (A)** Cyclic-voltammetry curve for nf-NCM. **(B)** Capacity versus voltage profile of all four samples. **(C)** Deconvoluted peaks from the cathodic and anodic peaks of the CV curve shown in Figure 3A. **(D)** Rate capability profile of all samples. **(E)** Capacity retention of all samples after 500 cycles of charge–discharge at 1,000 mA g⁻¹.
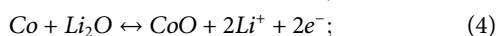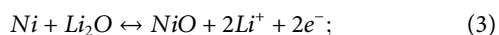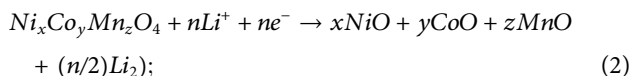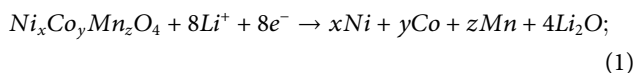
initial capacity loss. Indeed, the formation of respective metal oxide instead of their initial binary/ternary metal oxide was cited for the capacity loss in the conversion-type anode (Puthusseri et al., 2018). Cathodic peaks at 1.0–1.2 V can be observed from the second cycle onward. Four individual peaks were deconvoluted from this reduction peak (**Figure 3C**), which can be attributed to the formation of SEI as well as the conversion reaction for NiO→Ni, CoO→Co, and MnO→Mn (reaction #3–5). Deducted from the binding energy of each respective element, the deconvoluted reduction peaks at 1.03, 1.20, and 1.29 V for nf-NCM can be attributed to reduction reaction #3, #4, and #5, respectively. A broad peak can be observed during the

oxidation, which can also be further deconvoluted into three respective oxidation peaks (**Figure 3C**), with peaks at 1.73, 2.05, and 2.26 V corresponded to the oxidation reaction #5, #4, and #3, respectively. Despite the different role of each element in NCM cathode materials, nickel, cobalt, and manganese in NCM anode materials performed identical roles as the charge storage medium (reaction #3–5). Considering the destruction of the initial crystal phase during lithiation (reaction #1), the synergistic properties of nf-NCM would be lost, and each phase individually stores lithium ions during lithiation. Nevertheless, the synergistic effect could still be felt at the macroscale considering the homogenous distribution of these elements throughout the anode.
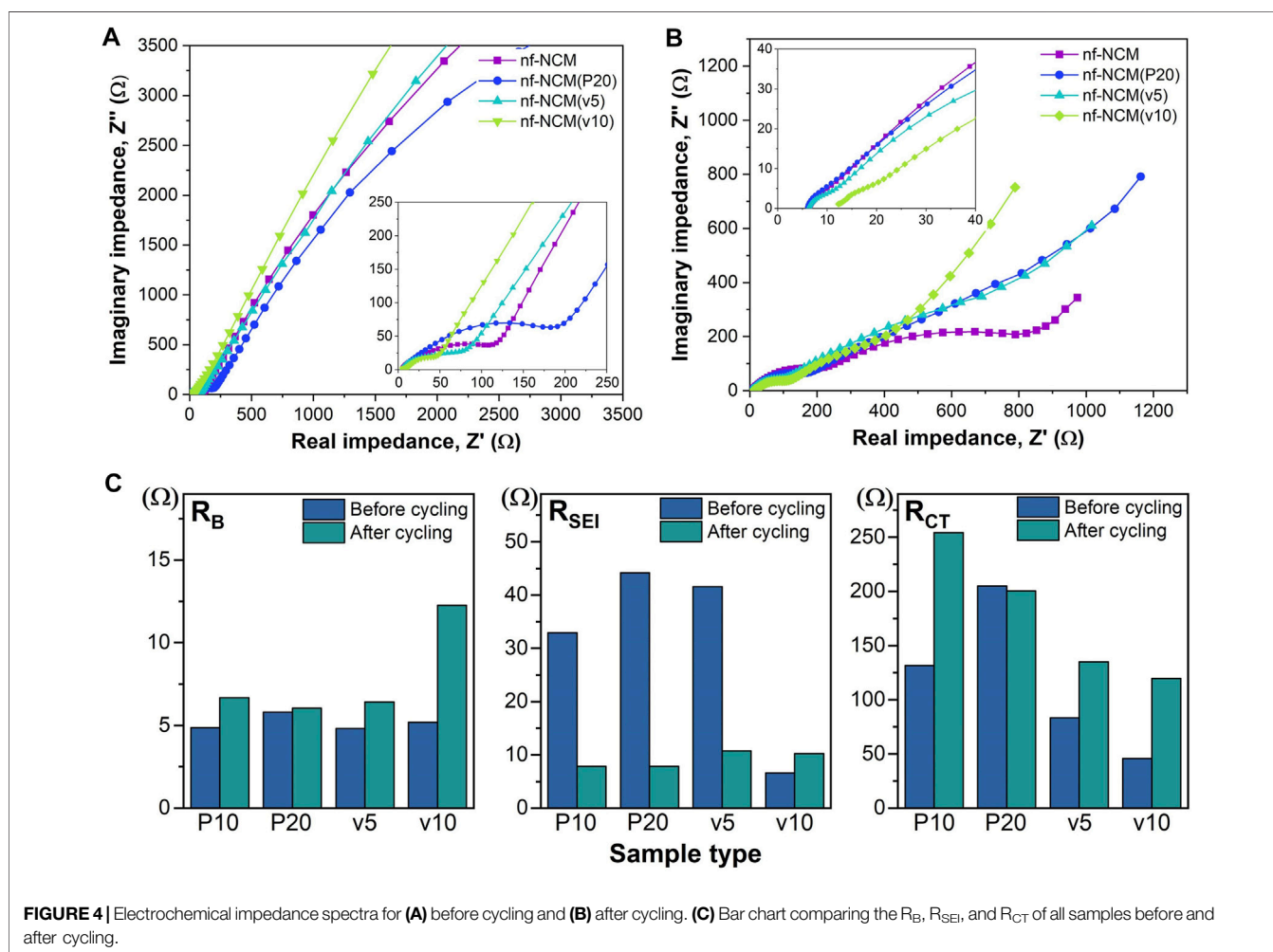
**TABLE 1 |** Impedance value extracted from electrochemical impedance spectra before and after stability cycling. The impedance value for post-formation is written in the bracket.

| Impedance | $R_B$ ($\Omega$) | $R_{SEI}$ ($\Omega$) | $R_{CT}$ ($\Omega$) |
|---|---|---|---|
| nf-NCM | 4.887 (6.676) | 32.91 (7.86) | 131.7 (254.29) |
| nf-NCM(P20) | 5.810 (6.039) | 44.16 (7.815) | 205.0 (200.52) |
| nf-NCM(v5) | 4.819 (6.412) | 41.56 (10.74) | 83.4 (135.09) |
| nf-NCM(v10) | 5.188 (12.270) | 6.64 (10.23) | 45.73 (119.75) |

$$Ni_xCo_yMn_zO_4 + 8Li^+ + 8e^- \rightarrow xNi + yCo + zMn + 4Li_2O; \tag{1}$$

$$Ni_xCo_yMn_zO_4 + nLi^+ + ne^- \rightarrow xNiO + yCoO + zMnO$$
$$+ (n/2)Li_2); \tag{2}$$

$$Ni + Li_2O \leftrightarrow NiO + 2Li^+ + 2e^-; \tag{3}$$

$$Co + Li_2O \leftrightarrow CoO + 2Li^+ + 2e^-; \tag{4}$$

$$Mn + Li_2O \leftrightarrow MnO + 2Li^+ + 2e^-. \tag{5}$$

The initial discharging capacity of 1074.8 mAh g$^{-1}$ is inferior to the theoretical capacity of 1760 mAh g$^{-1}$, which can be attributed

to the poor bulk resistance ($R_B$) as shown in **Table 1**. To probe into this matter, the ratio of conductive additive was increased to 20 wt.% where the nf-NCM was reduced to 70 wt.%, denoted as nf-NCM(P20), to increase the conductive pathway between individual fibers. By increasing the amount of conductive Super P, the initial discharge capacity of nf-NCM(P20) was enhanced to 1406.0 mAh g$^{-1}$ with a charging capacity of 861.4 mAh g$^{-1}$. Reduction in $R_B$ can be observed from impedance spectroscopy after cycling (**Figure 4**; **Table 1**), indicating that increasing the amount of conductive Super P ensured better connectivity between individual fibers and offered better electrochemical performance. We decided not to further increase the ratio of conductive Super P given that the high Super P content would increase the non-Faradaic contribution and reduce the specific capacity of the electrode. To further study the effect of interfiber connectivity on the electrochemical performance without further increasing the content of Super P, it was replaced by the vapor-grown carbon fiber (VGCF), denoted as nf-NCM(v5) and nf-NCM(v10). The discharging (charging) capacity was further enhanced to ~1663.6 (1039.0) and ~1810.4 (1114.8) mAh g$^{-1}$ for nf-NCM(v5) and nf-NCM(v10), respectively, which is in line with lower $R_{CT}$ recorded in the impedance spectra (**Table 1**). The value



**FIGURE 4 |** Electrochemical impedance spectra for **(A)** before cycling and **(B)** after cycling. **(C)** Bar chart comparing the $R_B$, $R_{SEI}$, and $R_{CT}$ of all samples before and after cycling.

of enhanced specific capacity is really close with the theoretical value of 1760 mAh g$^{-1}$, showing that poor interfiber connectivity is one of the main factors leading to the low-capacity value in nf-NCM.

The samples were also charged/discharged at varying current densities of ~200, ~400, ~800, and 1000 mA g$^{-1}$ to study their rate capability (**Figure 3D**). A higher content of conductive additives not only enhanced the specific capacity of nf-NCM but also its rate capability. When charged at 1000 mA·g$^{-1}$, nf-NCM, nf-NCM(P20), nf-NCM(v5), and nf-NCM(v10) could retain ~320.6, ~569.9, ~585.7, and ~534.0 mAh g$^{-1}$ corresponding to 52%, 65.6%, 66.5%, and 61.7%, respectively. The enhancement in rate capability of nf-NCM at a higher content of conductive additives can be attributed to better electrical conductivity within the fibers, which can be observed from the reduction in the charge transport impedance (R$_{CT}$) as shown in **Figure 4**; **Table 1**. Despite low R$_{CT}$, nf-NCM(v10) demonstrated slight reduction in capacity retention when de(charged) at 1000 mA g$^{-1}$ compared to nf-NCM(v5). Previous studies have reported that the synergistic effects of Super P and VGCF were required to improve the electrochemical performance of the LNCM cathode, where VGCF alone showed reduction in specific capacity as well as rate performance of the anode material (Cho et al.2015). Therefore, we anticipate that a higher content of VCGF could destroy the optimal synergistic effect between both conductive additives and could result in an increased R$_B$. The half-cells were then cycled at 1000 mA g$^{-1}$ for 500 cycles in the voltage range of 0.01 to 3 V for the stability test (**Figure 3E**). The nf-NCM could retain 54.2% of the initial capacity after 500 cycles of charge–discharging. The capacity retention of nf-NCM(P20), nf-NCM(v5), and nf-NCM(v10) were 57.3%, 52.7%, and 51.6%, respectively. From **Table 1**, we can observe that the SEI impedance (R$_{SEI}$) reduced when the ratio of conductive Super P was increased to 20 wt.%, indicating the formation of a more stable SEI layer and eventually leading to better cycling stability. However, incorporating VGCF into the conductive additives increased the R$_{SEI}$ drastically, where both nf-NCM(v5) and nf-NCM(v10) recorded R$_{SEI}$ of ~10 Ω. Despite lower R$_{CT}$ in nf-NCM(v5) and nf-NCM(v10), both higher R$_{SEI}$ and R$_B$ eventually lead to lower capacity retention in the VGCF-based samples. Even though VGCF could form a conductive network (Teng et al.2017), the ability for the conductive additives to self-distribute within the active materials was reported to play the most crucial role (Pfeifer et al.2020). The conductive carbon with smooth spherical morphology was reported to play a crucial role in ensuring good contact and formation of more stable SEI, which is in line with our observation. Therefore, despite lower R$_{CT}$, both higher R$_B$ and R$_{CT}$ counteracted the effect of better electronic conductivity of VGCF, leading to lower capacity retention during cycling. Obviously, increasing the content of conductive carbon boosted the electrochemical performance of electrospun nf-NCM, achieving specific capacity as high as ~1810.4 mAh g$^{-1}$ through the conversion process. However, the working voltage (~0.7 V) is still higher than that of conventional graphite (~10 mV), and understanding the origin of large potential hysteresis would be crucial in further improving the electrochemical performance of the nickel–cobalt–manganese oxide conversion-type anode.

## CONCLUSION

Nickel–cobalt–manganese oxide nanofibers are successfully fabricated using multi-needle electrospinning. The X-ray diffraction analyses showed that the quaternary metal oxide consists of multiple crystal phases, including $Co_2MnO_4$, $Ni_6MnO_8$, and NiO. Surface elemental analysis on the synthesized nanofibers showed that both Ni and Co ions coexisted in +2 and +3 state, whereas Mn, which functioned as the structure stabilizer through neutralizing additional charges, existed in +3 and +4 states. The electrochemical analysis showed that the synthesized quaternary metal oxide nanofibers offered a discharged capacity of ~1074.8 mAh g$^{-1}$, which was further improved to ~1810.4 mAh g$^{-1}$ by increasing the content of Super P as well as incorporation of VCGF. Electrochemical impedance analysis showed that such enhancement in discharge capacity can be attributed to the improved interfiber electrical connectivity. Deducted from the results, we can conclude that a higher ratio of conductive additives compared to the conventional ratio of 10 wt.% would be required to completely cover and connect nanostructures with a higher surface area, electrospun nanofibers in this case Goodenough, 2018.

## DATA AVAILABILITY STATEMENT

The original contributions presented in the study are included in the article/Supplementary Material; further inquiries can be directed to the corresponding authors.

## AUTHOR CONTRIBUTIONS

JL: study conception and design; JL, CK, and SD: data collection; JL and RJ: analysis and interpretation of results; JL, C-CY, and RJ: draft manuscript preparation; C-CY and RJ: project supervision. All authors reviewed the results and approved the final version of the manuscript.

## FUNDING

## ACKNOWLEDGMENTS

# REFERENCES

Bulavchenko, O. A., Venediktova, O. S., Afonasenko, T. N., Tsyrul'nikov, P. G., Saraev, A. A., Kaichev, V. V., et al. (2018). Nonstoichiometric Oxygen in Mn-Ga-O Spinels: Reduction Features of the Oxides and Their Catalytic Activity. *RSC Adv.* 8 (21), 11598–11607. doi:10.1039/c7ra11557a

Cao, K., Jin, T., Yang, L., and Jiao, L. (2017). Recent Progress in Conversion Reaction Metal Oxide Anodes for Li-Ion Batteries. *Mater. Chem. Front.* 1 (11), 2213–2242. doi:10.1039/c7qm00175d

Casimir, A., Zhang, H., Ogoke, O., Amine, J. C., Lu, J., and Wu, G. (2016). Silicon-based Anodes for Lithium-Ion Batteries: Effectiveness of Materials Synthesis and Electrode Preparation. *Nano Energy* 27, 359–376. doi:10.1016/j.nanoen.2016.07.023

Chemelewski, K. R., Li, W., Gutierrez, A., and Manthiram, A. (2013). High-voltage Spinel Cathodes for Lithium-Ion Batteries: Controlling the Growth of Preferred Crystallographic Planes through Cation Doping. *J. Mater. Chem. A.* 1 (48), 15334–15341. doi:10.1039/c3ta13265j

Chen, S., Zhang, X., Xia, M., Wei, K., Zhang, L., Zhang, X., et al. (2021). Issues and Challenges of Layered Lithium Nickel Cobalt Manganese Oxides for Lithium-Ion Batteries. *J. Electroanalytical Chem.* 895, 115412. doi:10.1016/j.jelechem.2021.115412

Cho, I., Choi, J., Kim, K., Ryou, M.-H., and Lee, Y. M. (2015). A Comparative Investigation of Carbon Black (Super-P) and Vapor-Grown Carbon Fibers (VGCFs) as Conductive Additives for Lithium-Ion Battery Cathodes. *RSC Adv.* 5 (115), 95073–95078. doi:10.1039/c5ra19056h

Cong, R., Choi, J.-Y., Song, J.-B., Jo, M., Lee, H., and Lee, C.-S. (2021). Characteristics and Electrochemical Performances of Silicon/carbon Nanofiber/graphene Composite Films as Anode Materials for Binder-free Lithium-Ion Batteries. *Sci. Rep.* 11 (1), 1283. doi:10.1038/s41598-020-79205-1

Dubey, P., Kaurav, N., Devan, R. S., Okram, G. S., and Kuo, Y. K. (2018). The Effect of Stoichiometry on the Structural, thermal and Electronic Properties of Thermally Decomposed Nickel Oxide. *RSC Adv.* 8 (11), 5882–5890. doi:10.1039/c8ra00157j

Fan, L., Zhang, W., Zhu, S., and Lu, Y. (2017). Enhanced Lithium Storage Capability in Li-Ion Batteries Using Porous 3D Co3O4 Nanofiber Anodes. *Ind. Eng. Chem. Res.* 56 (8), 2046–2053. doi:10.1021/acs.iecr.7b00222

Fang, S., Bresser, D., and Passerini, S. (2020). Transition Metal Oxide Anodes for Electrochemical Energy Storage in Lithium- and Sodium-Ion Batteries. *Adv. Energ. Mater.* 10 (1), 1902485. doi:10.1002/aenm.201902485

Goodenough, J. B. (2018). How We Made the Li-Ion Rechargeable Battery. *Nat. Electron.* 1 (3), 204. doi:10.1038/s41928-018-0048-6

Guanjie Li, G., Liao, Y., Li, Z., Xu, N., Lu, Y., Lan, G., et al. (2020). Constructing a Low-Impedance Interface on a High-Voltage LiNi0.8Co0.1Mn0.1O2 Cathode with 2,4,6-Triphenyl Boroxine as a Film-Forming Electrolyte Additive for Li-Ion Batteries. *ACS Appl. Mater. Inter.* 12 (33), 37013–37026. doi:10.1021/acsami.0c05623

He, L.-P., Li, K., Zhang, Y., and Liu, J. (2020). Structural and Electrochemical Properties of Low-Cobalt-Content LiNi0.6+xCo0.2-xMn0.2O2 (0.0 ≤ X ≤ 0.1) Cathodes for Lithium-Ion Batteries. *ACS Appl. Mater. Inter.* 12 (25), 28253–28263. doi:10.1021/acsami.0c06824

He, S., Huang, S., Wang, S., Mizota, I., Liu, X., and Hou, X. (2021). Considering Critical Factors of Silicon/Graphite Anode Materials for Practical High-Energy Lithium-Ion Battery Applications. *Energy Fuels* 35 (2), 944–964. doi:10.1021/acs.energyfuels.0c02948

Herrera-Gomez, A., Bravo-Sanchez, M., Ceballos-Sanchez, O., and Vazquez-Lepe, M. O. (2014). Practical Methods for Background Subtraction in Photoemission Spectra. *Surf. Interf. Anal.* 46 (10-11), 897–905. doi:10.1002/sia.5453

JinKiong, L., and Jose, R. (2021). Electrospun SnO2-CuO Semiconductor Composite Nanofibers and its Electrochemical Properties. *Mater. Today Proc.* 46, 1631–1634. doi:10.1016/j.matpr.2020.07.256

Kim, Y. (2012). Lithium Nickel Cobalt Manganese Oxide Synthesized Using Alkali Chloride Flux: Morphology and Performance as a Cathode Material for Lithium Ion Batteries. *ACS Appl. Mater. Inter.* 4 (5), 2329–2333. doi:10.1021/am300386j

Li, J. P. H., Zhou, X., Pang, Y., Zhu, L., Vovk, E. I., Cong, L., et al. (2019). Understanding of Binding Energy Calibration in XPS of Lanthanum Oxide by *In Situ* Treatment. *Phys. Chem. Chem. Phys.* 21 (40), 22351–22358. doi:10.1039/c9cp04187g

Liang, G., Peterson, V. K., See, K. W., Guo, Z., and Pang, W. K. (2020). Developing High-Voltage Spinel LiNi0.5Mn1.5O4 Cathodes for High-Energy-Density Lithium-Ion Batteries: Current Achievements and Future Prospects. *J. Mater. Chem. A.* 8 (31), 15373–15398. doi:10.1039/d0ta02812f

Ling, J., Karuppiah, C., Krishnan, S. G., Reddy, M. V., Misnon, I. I., Ab Rahim, M. H., et al. (2021a). Phosphate Polyanion Materials as High-Voltage Lithium-Ion Battery Cathode: A Review. *Energy Fuels* 35 (13), 10428–10450. doi:10.1021/acs.energyfuels.1c01102

Ling, J., Karuppiah, C., Reddy, M. V., Pal, B., Yang, C-C., and Jose, R. (2021b). Unraveling Synergistic Mixing of SnO2–TiO2 Composite as Anode for Li-Ion Battery and Their Electrochemical Properties. *J. Mater. Res.* 36, 4120–4130. doi:10.1557/s43578-021-00313-3

Manthiram, A. (2020). A Reflection on Lithium-Ion Battery Cathode Chemistry. *Nat. Commun.* 11 (1), 1550. doi:10.1038/s41467-020-15355-0

Mizushima, K., Jones, P. C., Wiseman, P. J., and Goodenough, J. B. (1980). LixCoO2 (0. *Mater. Res. Bull.* 15 (6), 783–789. doi:10.1016/0025-5408(80)90012-4

Moon, J., Lee, H. C., Jung, H., Wakita, S., Cho, S., Yoon, J., et al. (2021). Interplay between Electrochemical Reactions and Mechanical Responses in Silicon-Graphite Anodes and its Impact on Degradation. *Nat. Commun.* 12 (1), 2714. doi:10.1038/s41467-021-22662-7

Musuvadhi Babulal, L., Yang, C. C., Wu, S.-h., Chien, W.-C., Jose, R., and Jessie Lue, S. (2021). Enhanced Performance of a Ni-Rich LiNi0.8Co0.1Mn0.1O2 Cathode Material Formed through Taylor Flow Synthesis and Surface Modification with Li2MoO4. *Chem. Eng. J.* 413, 127150. doi:10.1016/j.cej.2020.127150

Pfeifer, K., Arnold, S., Budak, Ö., Luo, X., Presser, V., Ehrenberg, H., et al. (2020). Choosing the Right Carbon Additive Is of Vital Importance for High-Performance Sb-Based Na-Ion Batteries. *J. Mater. Chem. A.* 8 (12), 6092–6104. doi:10.1039/d0ta00254b

Puthusseri, D., Wahid, M., and Ogale, S. (2018). Conversion-type Anode Materials for Alkali-Ion Batteries: State of the Art and Possible Research Directions. *ACS Omega* 3 (4), 4591–4601. doi:10.1021/acsomega.8b00188

Seenivasan, M., Yang, C.-C., Wu, S.-h., Chien, W.-C., Wu, Y.-S., Jose, R., et al. (2021). Using a Couette-Taylor Vortex Flow Reactor to Prepare a Uniform and Highly Stable Li[Ni0·80Co0·15Al0.05]O2 Cathode Material. *J. Alloys Comp.* 857, 157594. doi:10.1016/j.jallcom.2020.157594

Solmaz, R., Karahan, B. D., and Keles, O. (2020). Fabrication of Nickel Manganese Cobalt Oxide (NMCO) Anodes for Lithium-Ion Batteries via Hydrothermal Process. *J. Appl. Electrochem.* 50 (10), 1079–1089. doi:10.1007/s10800-020-01462-9

Song, L., Du, J., Xiao, Z., Jiang, P., Cao, Z., and Zhu, H. (2020). Research Progress on the Surface of High-Nickel Nickel-Cobalt-Manganese Ternary Cathode Materials: A Mini Review. *Front. Chem.* 8 (761), 761. doi:10.3389/fchem.2020.00761

Teng, X., Xu, H.-l., Liu, Q., Shi, L.-l., Gai, L., Wang, L., et al. (2017). The Influence of Conductive Additives on the Performance of a SiO/C Composite Anode in Lithium-Ion Batteries. *New Carbon Mater.* 32 (6), 572–580. doi:10.1016/s1872-5805(17)60138-0

Tolouei, A., Kaflou, A., and Sadrnezaad, S. K. (2019). Effects of Lithium Excess and Ni Content on the Electrochemical Performance of Li1+x (Ni0.45−xMn0.4Co0.15) O2 Lithium-Ion Cathode Materials in Stoichiometric State. *Mater. Res. Express* 6 (8), 085522. doi:10.1088/2053-1591/ab2019

Wang, T., Ren, K., He, M., Dong, W., Xiao, W., Pan, H., et al. (2020). Synthesis and Manipulation of Single-Crystalline Lithium Nickel Manganese Cobalt Oxide Cathodes: A Review of Growth Mechanism. *Front. Chem.* 8 (747), 747. doi:10.3389/fchem.2020.00747

Wangda Li, W., Liu, X., Xie, Q., You, Y., Chi, M., and Manthiram, A. (2020). Long-Term Cyclability of NCM-811 at High Voltages in Lithium-Ion Batteries: an In-Depth Diagnostic Study. *Chem. Mater.* 32 (18), 7796–7804. doi:10.1021/acs.chemmater.0c02398

Wu, Y.-S., Pham, Q.-T., Yang, C.-C., Chern, C.-S., Musuvadhi Babulal, L., Seenivasan, M., et al. (2021). Study of Electrochemical Performance and thermal Property of LiNi0.5Co0.2Mn0.3O2 Cathode Materials Coated with

a Novel Oligomer Additive for High-Safety Lithium-Ion Batteries. *Chem. Eng. J.* 405, 126727. doi:10.1016/j.cej.2020.126727

Xu, C., Dai, Q., Gaines, L., Hu, M., Tukker, A., and Steubing, B. (2020). Future Material Demand for Automotive Lithium-Based Batteries. *Commun. Mater.* 1 (1), 99. doi:10.1038/s43246-020-00095-x

Yang, Y., Yuan, W., Kang, W., Ye, Y., Pan, Q., Zhang, X., et al. (2020). A Review on Silicon Nanowire-Based Anodes for Next-Generation High-Performance Lithium-Ion Batteries from a Material-Based Perspective. *Sust. Energ. Fuels* 4 (4), 1577–1594. doi:10.1039/c9se01165j

Yim, C.-H., Courtel, F. M., and Abu-Lebdeh, Y. (2013). A High Capacity Silicon-Graphite Composite as Anode for Lithium-Ion Batteries Using Low Content Amorphous Silicon and Compatible Binders. *J. Mater. Chem. A.* 1 (28), 8234–8243. doi:10.1039/c3ta10883j

Yue, J., Badaczewski, F. M., Voepel, P., Leichtweiß, T., Mollenhauer, D., Zeier, W. G., et al. (2018). Critical Role of the Crystallite Size in Nanostructured Li4Ti5O12 Anodes for Lithium-Ion Batteries. *ACS Appl. Mater. Inter.* 10 (26), 22580–22590. doi:10.1021/acsami.8b05057

Zhang, H., Xu, J., and Zhang, J. (2019). Surface-Coated LiNi0.8Co0.1Mn0.1O2 (NCM811) Cathode Materials by Al2O3, ZrO2, and Li2O-2B2O3 Thin-Layers for Improving the Performance of Lithium Ion Batteries. *Front. Mater.* 6 (309). doi:10.3389/fmats.2019.00309

Zhang, X., Wang, D., Qiu, X., Ma, Y., Kong, D., Müllen, K., et al. (2020). Stable High-Capacity and High-Rate Silicon-Based Lithium Battery Anodes upon Two-Dimensional Covalent Encapsulation. *Nat. Commun.* 11 (1), 3826. doi:10.1038/s41467-020-17686-4

Zuo, X., Zhu, J., Müller-Buschbaum, P., and Cheng, Y.-J. (2017). Silicon Based Lithium-Ion Battery Anodes: A Chronicle Perspective Review. *Nano Energy* 31, 113–143. doi:10.1016/j.nanoen.2016.11.013